Low Temperature Plasma
Technology Laboratory

Nonlinear effects and anomalous transport in rf plasmas

Francis F. Chen

LTP-506 June, 2005

Electrical Engineering Department
Los Angeles, California 90095-1594

Nonlinear effects and anomalous transport in rf plasmas

Francis F. Chen

University of California, Los Angeles, California *90095*

ABSTRACT

Three examples are given of experiments which give evidence of nonclassical behavior in partially ionized, low-temperature, radiofrequency (rf) plasmas: anomalous skin depth in inductively coupled plasmas (ICPs), transport by fluctuations in helicon plasmas, and parametric instabilities in helicon plasmas. A variety of physics puzzles have been found in industrial plasmas, and techniques learned from high-temperature, fusion research are used to solve them. Low-temperature plasma physics is becoming a precise, challenging discipline in the field of plasmas.

Although plasmas were first studied in weakly ionized discharges such as glow discharges, the explosion of knowledge of how plasmas behave and how they can be diagnosed has come from the fusion effort. Hot, collisionless plasmas provide a certain degree of simplicity which allowed progress to proceed. Partially ionized plasmas, which add to the ions and electrons a neutral species with many energy levels were regarded as too complicated, leading to "dirty science". This is not always true, of course. Partially ionized plasmas do not have to be in a confinement geometry and, indeed do not need a dc magnetic field, so are in many ways simpler. Plasmas being what they are, even cold plasmas produce the anomalous and nonlinear effects seen in hot plasmas. Three examples of interesting problems are given here. These do not include sheaths, which are inescapably nonlinear (but may not be plasmas) and in any case are less interesting than these other problems.

I. Anomalous skin depth in ICPs

ICPs are plasma sources excited with an external antenna carrying an rf current, usually at the industrial frequency of 13.56 MHz. They are one of the main plasma devices used in producing computer chips and are therefore highly developed. But they were developed without a good understanding of how they worked. There are two basic types of antennas. The first is a spiral coil shaped like a stove-top heating element and placed on the dielectric top cover of a vacuum chamber. After breakdown, the rf field from the antenna current penetrates about a skin depth into the plasma and creates the ionization there. The plasma diffuses a short distance downwards to the substrate to be treated. There is no problem understanding this. The second type of antenna, however, is wound around the cylindrical sides of the vacuum chamber, with no elements near the axis. Since the skin depth is much smaller than the chamber radius, one would expect ionization to occur near the sidewalls, with the plasma diffusing toward the axis. Since particles are lost to the top and bottom by thermal motion while they are diffusing, one would expect the density to peak near the sidewalls and have a minimum on the axis. Figure 1 shows that the opposite happens[1]. The rf field decays inward with the expected e-folding length, and KT_e peaks in the skin layer, as expected. The density n, however, has a minimum in the skin layer and peaks near the center. In commercial use, the parameters can be adjusted to produce a completely uniform plasma across the diameter.

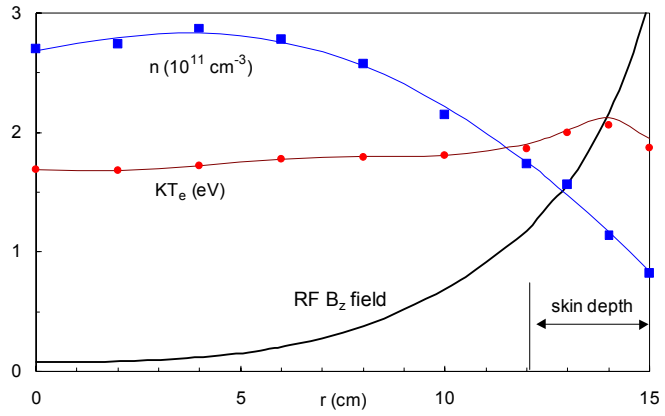

Fig. 1. Radial profiles of density, electron temperature, and the rf B_z field in the apparatus of Fig. 2. [Ref.1]

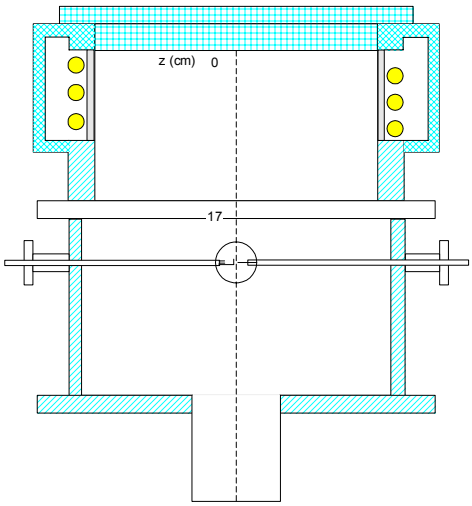

Fig. 2. Schematic of a commercial processing reactor with a side-mounted antenna.

The rf energy has apparently penetrated beyond the classical skin depth and has produced ionization in the interior of the discharge. This problem of anomalous skin depth in plasmas has been known for many years since it was reported by Demirkhanov et al.[2] and Kofoid and Dawson[3], and later by Joye and Schneider[4]. Weibel[5], and later Sayasov[6], proposed theoretically that electron thermal motions could transport rf energy past the skin layer. With the advent of ICPs, the subject was revived in the 1990s. This literature has been summarized in three long review articles by Kolobov and Economou[7] (theory), Kolobov and Godyak[8], and Godyak[9] (experiment). Most papers[10-13] consider ICPs with flat-coil antennas. Since these impose rf fields on axis, the problem of peaked density profiles does not arise, as with side-mounted antennas [Fig. 2]. These papers therefore do not bear on the present problem. On the other hand, Godyak et al. have discovered nonlinear effects in ICPs which may be important. For instance, there are regions of negative absorption in which electrons heated in the skin layer move thermally away and deposit their energy after the rf has changed phase.[14] Collisionless absorption can be 10 times larger than collisional absorption. Furthermore, the ponderomotive force $\mathbf{F}_{\mathrm{NL}}$ was found to generate 2ω oscillations[15,16] at twice the rf frequency as well as a nonlinear dc force.[17,18,19] The former penetrates somewhat deeper into the plasma, and the latter can change the equilibrium profiles. At frequencies below 500 kHz, the 2ω force can be larger than the dc force.[20] These nonlinear effects have been treated neatly by Smolyakov et al.[21], who also consider cylindrical geometry. In purely inductive discharges, the ponderomotive force $\mathbf{F}_{\mathrm{NL}}$ on a single electron is the same as the nonlinear Lorentz force

$$\mathbf{F}_{\mathrm{L}} = -e\tilde{\mathbf{v}} \times \tilde{\mathbf{B}}. \tag{1}$$

If an electrostatic field is also present, however, $\mathbf{F}_{\mathrm{NL}}$ takes the form[18,19,21,22]

$$\mathbf{F}_{NL} = -\frac{e^2}{2m\omega^2}\left[(\mathbf{E}\cdot\nabla)\mathbf{E} + \mathbf{E}\times(\nabla\times\mathbf{E})\right] = -\frac{e^2}{4m\omega^2}\nabla\,|\,\mathbf{E}\,|^2, \tag{2}$$

where the second term comes from Eq. (1) and is partially canceled by the first term, an effect omitted in earlier papers[15]. Smolyakov et al.[18,19] found that Eq. (2) has to be modified by thermal effects in order to agree with experiment. They also pointed out[21] that electrostatic fields arise from polarization drifts. These drifts also cancel the effect of a dc magnetic field $\mathbf{B}_0$ on the skin depth[21], a surprising effect also found by Chen[23]. Changes in the electron energy distribution caused by nonlinear effects and by thermal diffusion have been observed in meticulous experiments by Godyak et al.[12,24,25]

We believe that the explanation of peaked or flat density profiles with side-mounted antennas requires both cylindrical geometry and nonlinearity[1]. Several other papers, to be discussed later, have also included both these effects. To see how primary electrons can reach the discharge interior, we can follow the trajectory of an electron through several rf cycles (Fig. 3). Consider an electron which starts inside the skin layer and is accelerated as the rf E_θ-field rises in the clockwise direction. The shorter trajectory is computed neglecting the nonlinear Lorentz force $\mathbf{F}_{\mathrm{L}}$ [Eq. (1)], where $\tilde{\mathbf{v}}$ and $\tilde{\mathbf{B}}$ are both at the rf frequency. The electron is assumed to be specularly reflected at the wall sheath of negligible thickness. In this case, the electron remains in the skin layer as it speeds up, and wanders into the interior only after the rf reverses direction and slows the electron down. The longer path includes the effect of $\mathbf{F}_{\mathrm{L}}$. Since the main component of $\tilde{\mathbf{B}}$ is B_z, and that of $\tilde{\mathbf{v}}$ is v_θ, $\mathbf{F}_{\mathrm{L}}$ is in the r direction, causing the electrons to hit the wall sheath at a steeper angle. This quickly brings the electron into the central region, from

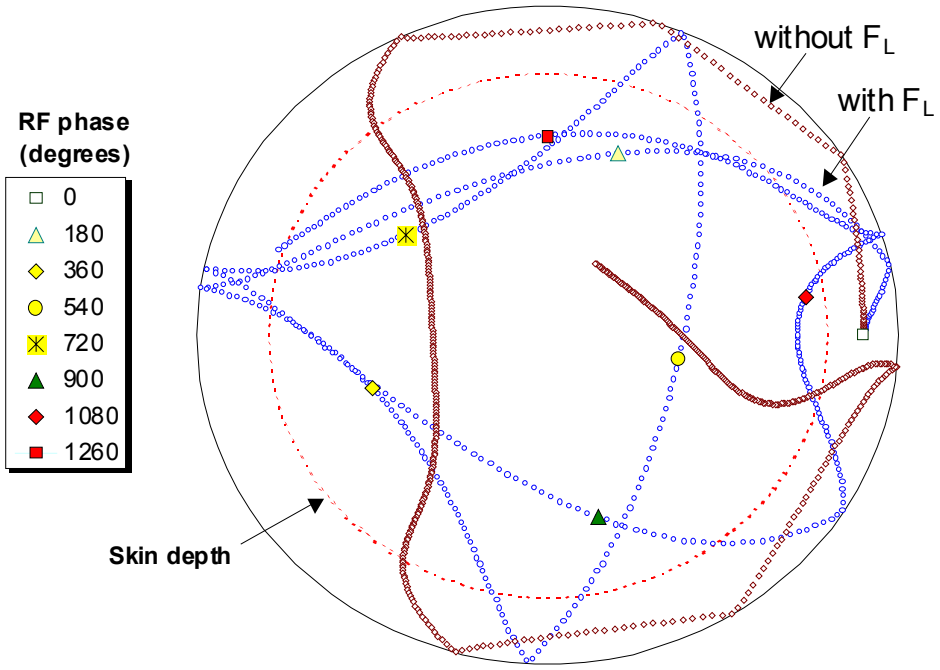

Fig. 3. Trajectory of an electron through four rf cycles [Ref. 1]. Assumed parameters: f = 6.78 MHz, skin depth = 3.1 cm, tube radius = 15 cm, sheath drop = 20 V, p = 10 mTorr (argon), and KT_e = 3 eV.

which the electron can enter the skin layer at a steep angle even without further help from $\mathbf{F}_L$. One sees from the spacing of the time steps that the electron can travel to the interior while it still has a large energy and therefore can produce ionization there. This is shown more clearly in Fig. 4, where the electron energy E with and without $\mathbf{F}_L$ is plotted for the first four rf cycles. Without $\mathbf{F}_L$, E is above the ionization threshold of argon only while the electron is in the skin layer,

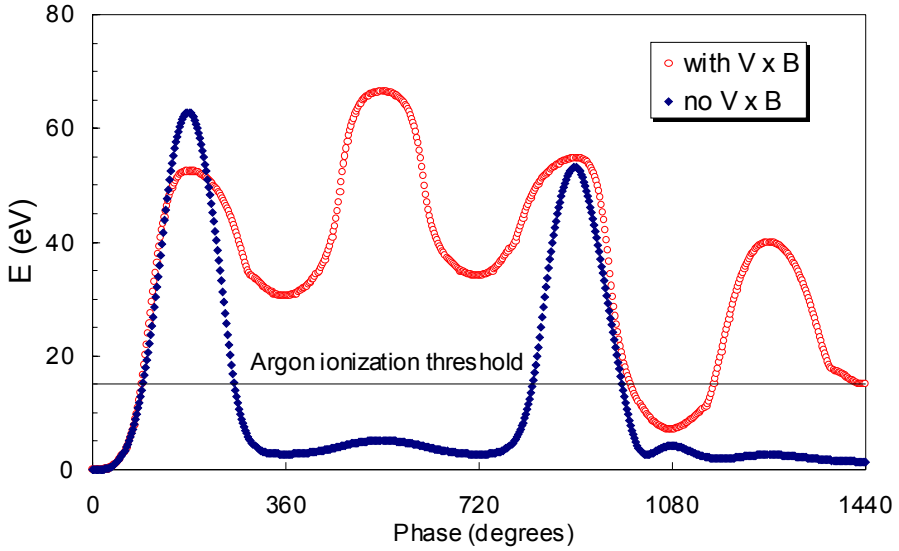

Fig. 4. Energy of the test electron computed with (○)and without (♦) the Lorentz force, for an applied rf E-field of 8 V/cm at 6.78 MHz. [Ref. 1]

while inclusion of $\mathbf{F}_L$ brings E above the threshold in almost all phases of the rf. To do a realistic calculation, Evans and Chen[1] followed the electron through 32,000 time steps over many rf

cycles. The rf *E*-field was given a radial profile according to classical skin-depth theory. Both elastic and inelastic collisions of the electron with neutrals and ions were included. When the

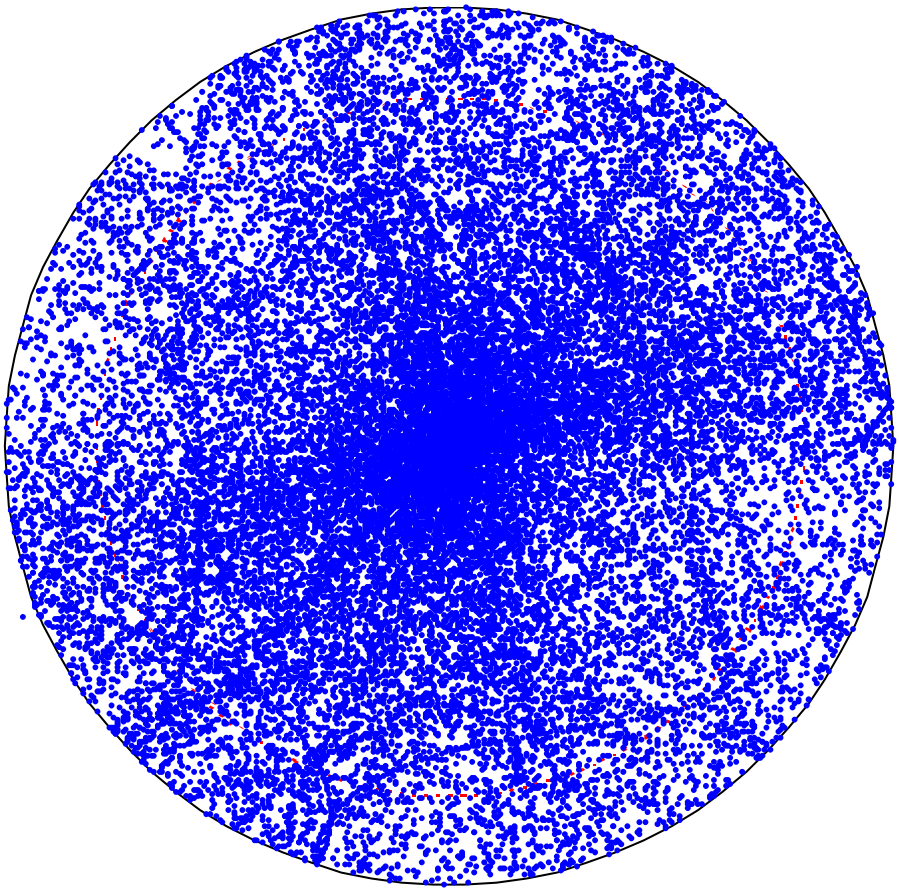

Fig. 5. Distribution of electron positions after 32,000 2-nsec time steps. [Ref. 1]

electron enters the sheath with a perpendicular energy larger than the normal sheath drop, it was not reflected but was absorbed. It was then re-injected into the discharge at an arbitrary position and given a random energy according to the temperature of the bulk electrons. Figure 5 is a plot of these 32,000 positions, which also represent the distribution of electron density. The density is peaked on axis for two reasons. First, when the orbit crosses itself, it tends to enhance the density of dots at small radii, where the area is small. Second, when electrons are re-injected into the interior of the discharge, they spend a long time there before reaching the skin layer, where they can get accelerated.

The density distribution can be obtained by dividing the circle into four ring-shaped sectors of equal area and counting the dots in each. The result is shown in Fig. 6: the density is peaked at the center. Overlaid on this is the measured curve of Fig. 1, which has a similar shape, though the calculation was not made with the exact experimental conditions; in particular, it was a 2D calculation only. The energy distribution in each sector can also be obtained from the calculation. This is shown in Fig. 7. A Maxwellian appears as a curve on this log-log scale. It is clear that a high-energy tail is available in each region, including the one on axis, to produce ionization events.

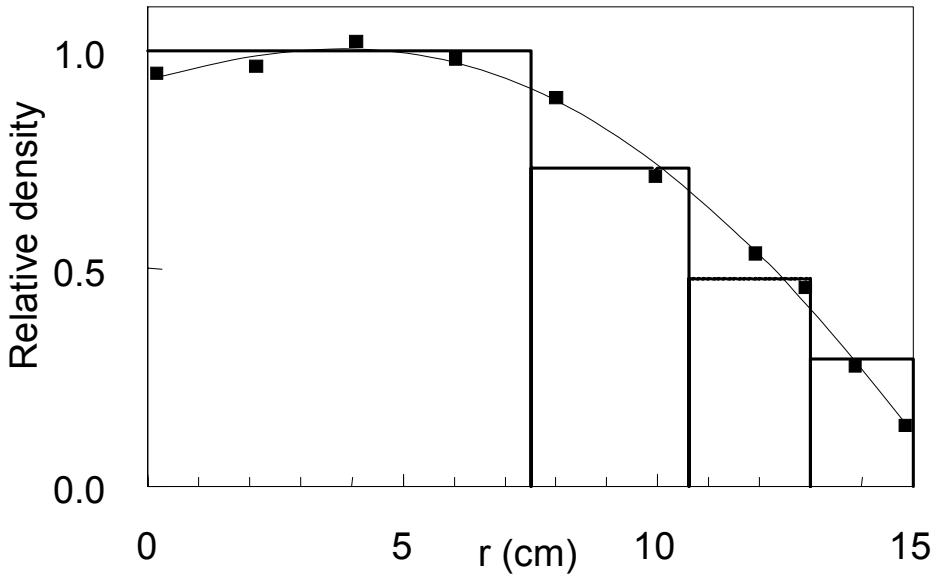

Fig. 6. Histogram of the density distibution of Fig. 5, together with the experimental curve of Fig. 1. [Ref. 1]

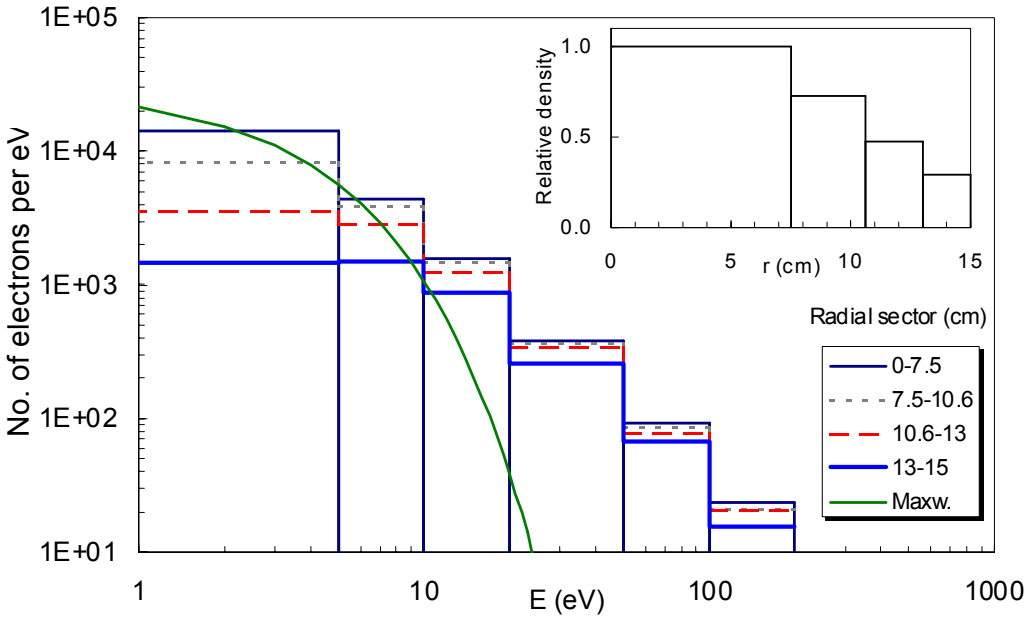

Fig. 7. Calculated energy distributions in each sector, compared with a Maxwellian (curve), on a log-log scale. The radii covered by each sector are shown in the inset. [Ref. 1]

Another radial force which could enhance the angle-sharpening effect is the dc ambipolar electric field E_{amb}. We have neglected this for two reasons. First, the classical formula for E_{amb} is not always followed, since electrons have a tendency to follow the Boltzmann relation, which leads to a slightly different profile for $E_{amb}(r)$. Second, the force $-e\mathbf{E}_{amb}$ is much smaller than $\mathbf{F}_L = -e(\mathbf{v} \times \mathbf{B})$. The computations above used a reasonable rf amplitude B of 7 G = 7×10^{-4} T. Electrons accelerated to an ionizing energy of, say, 20 eV have velocities $\sim 2.7 \times 10^6$ m/sec. The magnitude of $|\mathbf{v} \times \mathbf{B}|$ is, therefore, of order 2000 V/m. The ambipolar field is given by

$$\mathbf{E}_{amb} \approx -\frac{D_e}{\mu_e}\frac{\nabla n}{n} = -\frac{KT_e}{e}\frac{\nabla n}{n} \approx -\hat{\mathbf{r}}\frac{KT_e}{ea}, \tag{3}$$

where $a \sim 0.15$m is the chamber radius. For $KT_e = 3$eV, this yields $|\mathbf{E}_{amb}| \sim 20$ V/m, two orders smaller than $|\mathbf{v} \times \mathbf{B}|$. Of course, $\mathbf{F}_L$ is large only in the skin, and its average there is only 63% of its maximum, while $\mathbf{E}_{amb}$ is applied for a distance a, or at least a mean free path. On the other hand, since we are concerned about density profiles in ICPs that are essentially flat, $\mathbf{E}_{amb}$ vanishes with $\nabla n / n$. In any case, the two forces have very different magnitudes.

The importance of the rf field $\tilde{\mathbf{B}}$ was first pointed out in a series of papers by Rognlien et al.[26-29] Extensive numerical calculations treated not only the effect of $\tilde{\mathbf{B}}$ on the radial velocities but also the changes in dc profiles caused by this. The orbit changes were found to lower the density, changing a peaked density profile into a flat one. However, the profile shown was for slab geometry and may not pertain to cylinders. An elegant paper by Kolobov et al.[30] treated both cylindrical geometry and the nonlinear Lorentz force. They tackled the problem both analytically and computationally in a Monte Carlo calculation with prescribed skin fields, as was done here. The effect shown here was certainly contained in their work, though their emphasis was on the radial energy gain rather than the density profile.

The anomalous penetration of rf energy with side-mounted antennas can therefore be explained by the angle-sharpening effect of the nonlinear Lorentz force term. For explaining flat density profiles, we believe that this is a strong physical mechanism which stands out over all other effects considered in previous papers. In practice, electrons have thermal motions in the z direction, which would cause them to be lost axially as they diffuse inward. This loss of particles in the z direction depends on the aspect ratio of the chamber and is included neither by Evans and Chen[1] nor by previous workers[28,30]. It would make weaker mechanisms incapable of avoiding the density hole that one would expect on axis. A full calculation would have to account for three dimensions in both position and velocity, and would have to be done on the electron time scale.

Anomalous skin depth has a second aspect which is not experimentally important but is intriguing. It can be seen in the radial plot of rf B_z field shown in Fig. 8. The field decays exponentially (actually, an I_0 Bessel function) away from the antenna, but then deviates from the

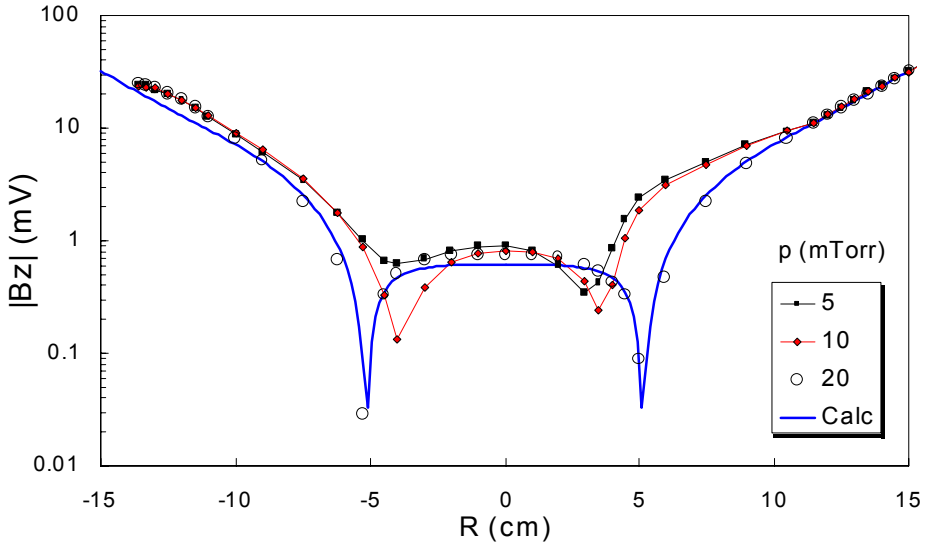

Fig. 8. Radial profiles of rf B_z field at various pressures. The bottom curve is a computed fit to the 20-mTorr data [Ref. 1]. Experimental conditions: 400 W at 2 MHz, 5–20 mTorr of Ar.

straight line after reaching a few percent of the initial amplitude. It goes to a minimum and rises again at the axis with reversed phase. It behaves like a standing wave, but no such effect is predicted by electromagnetic theory. As is seen in Fig. 8, the effect is actually larger at larger pressure. This non-monotonic behavior has been seen many times previously[14,11,9,31], mostly with flat-coil antennas, and it has been explained by thermal diffusion of electrons away from the antenna while retaining the phase of the previous half-cycle. Evans and Chen[1] have proposed a slightly different picture of this mechanism. The azimuthal current in the skin layer can break free to form a detached ring current which is pushed inwards by the ponderomotive force. Such a current ring would have its own L / R decay time, different from the driven reversal of the rf field. Thus, it can have a reversed phase by the time it reaches the interior of the discharge. Figure 9 shows the field of the current ring at its final radius before it decays or bounces outwards due to the internal field pressure. This geometry resembles that of a spherical tokamak, but this is a transient rf structure. The field lines are not sketches; they were computed assuming an aspect ratio and a current profile of the ring[1]. The L / R time was computed from the calculated inductance of the structure and the electron collison rate. The parameters can be adjusted to give a B_z curve fitting the data in Fig. 8.

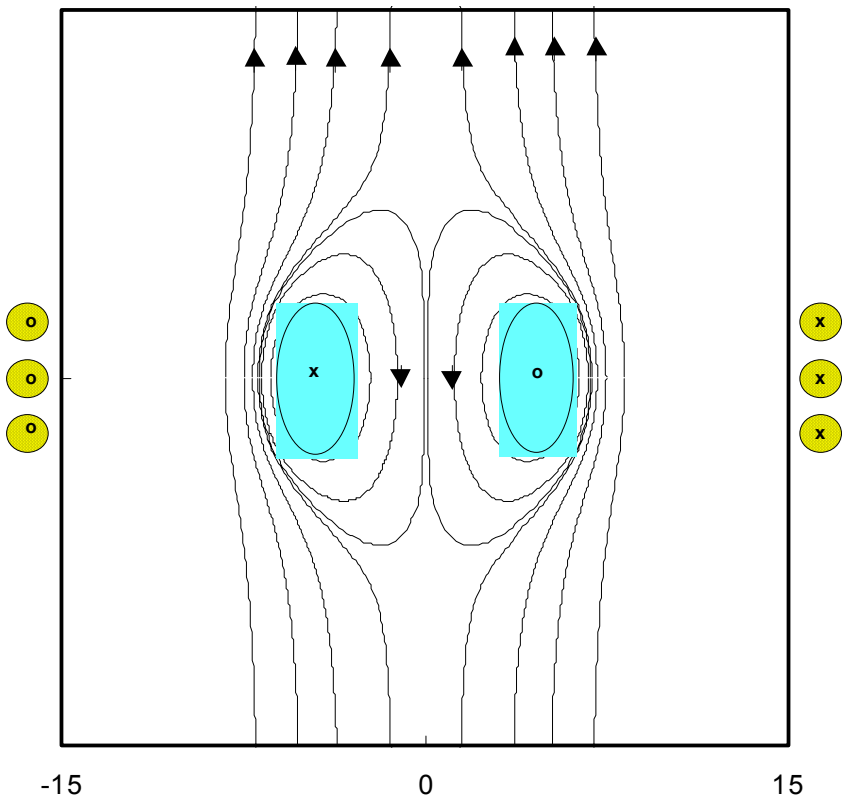

Fig. 9. A detached current ring and its B-field in a plasma. The field of the external antenna has been added to that generated by the current ring [Ref. 1]. Assumed conditions: $n = 8 \times 10^{10}$ cm^{-3} plasma with $p = 10$ mTorr, $KT_e = 3$ eV, and $f = 2$ MHz.

We have shown that a simple device like an ICP can operate in a quite complicated way. Both the anomalous rf penetration and reversed field effects should appear in a full simulation containing the essential physics. Such a simulation will tell whether or not our conjectures are correct, but this has not been done yet.

II. Anomalous transport in helicon plasmas

Like ICPs, helicon discharges are excited by an external rf antenna, but the energy coupling is entirely different. A dc magnetic field is required. In this field, the antenna excites a whistler wave propagating along a cylinder coaxial with the *B*-field. A helicon wave differs from a whistler wave in free space because it is confined within a cylinder, and the reflections change the entire mode structure of the wave. Energy coupling is not simply by collisional damping, which is weak, but by mode coupling to a strongly damped wave. Details will not be required until the next section. In simplest terms, helicons follow the low-frequency, high-density limit of the whistler dispersion relation, which can be written as follows:

$$k_\perp^2 + k_\parallel^2 \approx k_\perp^2 = \frac{\omega}{k_\parallel}\frac{ne\mu_0}{B_0}. \tag{4}$$

In cylindrical geometry, $k_\perp$ is set by the tube radius and the azimuthal mode number, and $k_\parallel \equiv k$ is set by the antenna length. With these constants, one sees that n should increase linearly with B_0. Deviations from this relationship have been found, especially with light elements, as shown in Fig. 10[32]. With argon and neon, n grows linearly with B_0 but saturates above a critical field B_{crit}. With hydrogen and helium, n peaks and then falls at higher field. Light et al.[32] found that B_{crit}

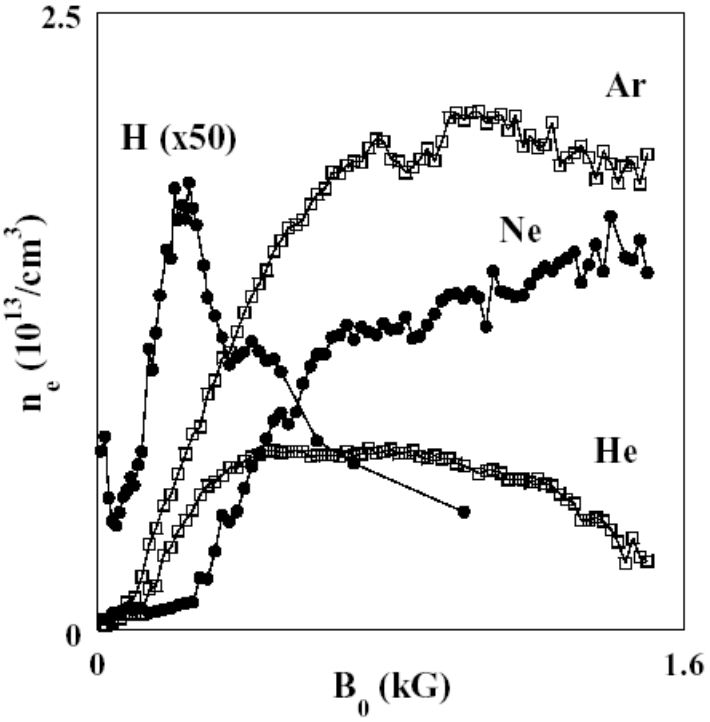

Fig. 10. Helicon density on axis for various gases vs. magnetic field. [Ref. 32]

coincides with the onset of an instability. In Fig. 11, the spectrum of ion current oscillations on a probe is plotted against *B*-field. At around 600 G, where the density begins to saturate, discrete modes can be seen in the spectrum below 10 kHz. These evolve into a turbulent spectrum at higher fields, where n has saturated. The low frequency of the oscillations, falling with B_0, suggests resistive drift waves; but since the radial *E*-field is sheared, Kelvin-Helmholtz instabilities are also possible. Light[33] derived the dispersion relation of combined K-H and drift

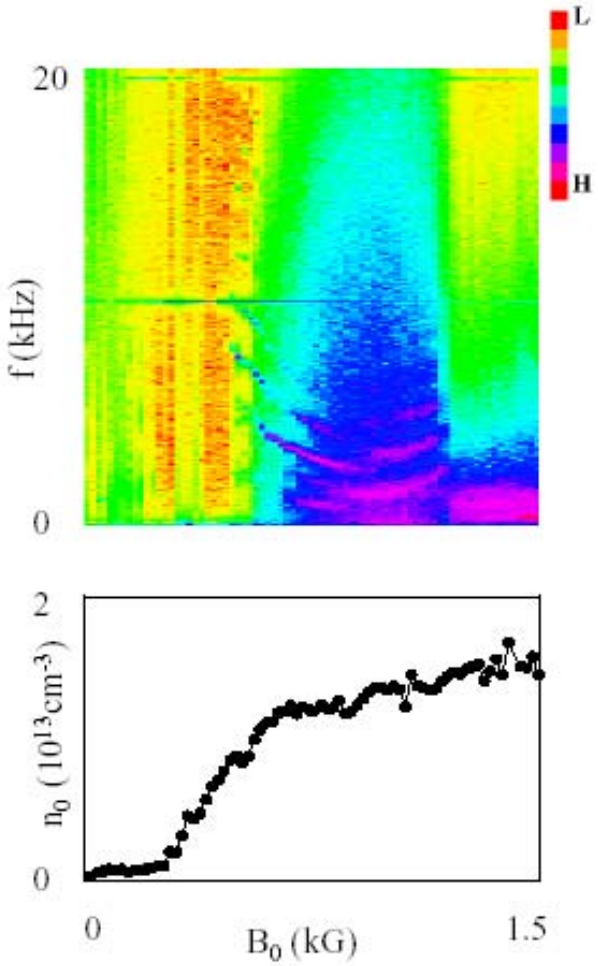

Fig. 11. Bottom: density vs. B_0 measured in neon. Top: frequency spectrum of probe signals on same scale. [Ref. 32]

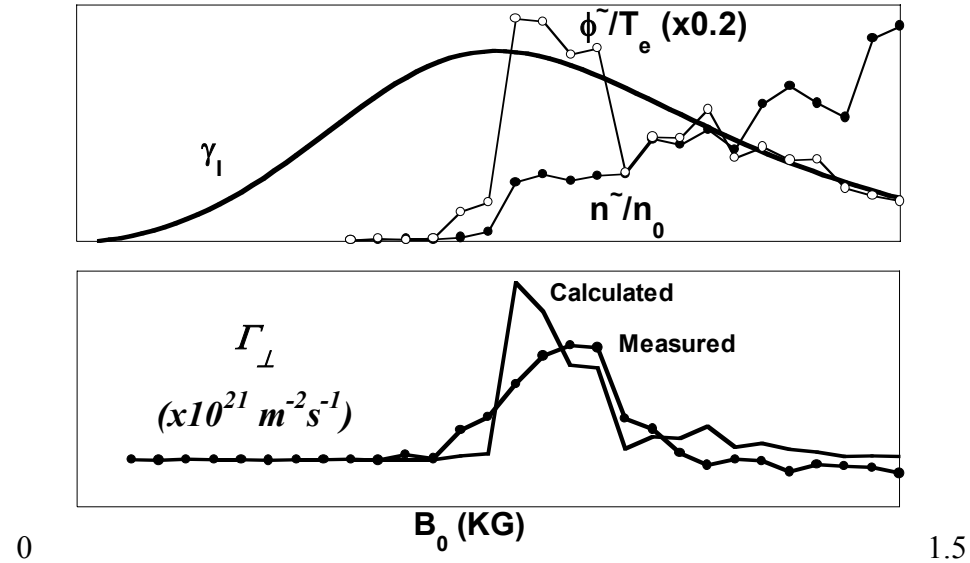

Fig. 12. Top: Computed growth rate vs. $\mathbf{B}_0$ compared with measured potential and density fluctuation amplitudes. Bottom: Calculated and measured radial transport fluxes. [Ref. 33]

waves and calculated the threshold and growth rate using the measured equilibrium conditions. The results are shown in Fig. 12 for helium. The normalized potential and density fluctuation amplitudes $\tilde{\phi}$ and $\tilde{n}$ are seen to rise at the magnetic field where the computed growth rate γ is maximum. Thus, the instability was identified both from the wave's propagation characteristics and from its growth rate in relation to the onset of turbulence.

The next step is to measure the transport caused by the instability. A triple-probe array was used[34], with one probe biased to collect ion current and the two others floating to measure potential fluctuations, from which $\tilde{E}$ could be obtained. The floating probes were capacitance neutralized to obtain sufficient frequency response at high impedance. The radial flux $\Gamma_\perp$ was computed using standard $<\tilde{n}\,\tilde{\phi}>$ or $<\tilde{n}\,\tilde{E}>$ correlation techniques and is shown vs. B_0 in the bottom half of Fig. 12. Also shown is $\Gamma_\perp$ computed from the theoretical phase shift and the measure amplitudes. These are in reasonable agreement. There is, however, one flaw in the ointment. At the fields at which the oscillations are largest, the radial flux occurs only at mid-radius; it does not exist near the edge (Fig. 13). Some kind of transport barrier stabilizes the plasma near the boundary. In toroidal confinement, this would lead to an H-mode density increase, but here the plasma is bounded at the ends. Axial flow can transport the plasma to the endplates. Measurements using Mach probes did detect a large axial flow in the outer regions of the discharge. Thus, the transport mechanism in this finite-length plasma is rather complicated. Oscillatory transport brings plasma from the inside, where the cross-sectional area is small, to the outside, where there is more area. There, the oscillations are stabilized, possibly because of electric-field shear, and the density piles up. The plasma is then forced by the density gradient to transport itself axially to the ends.

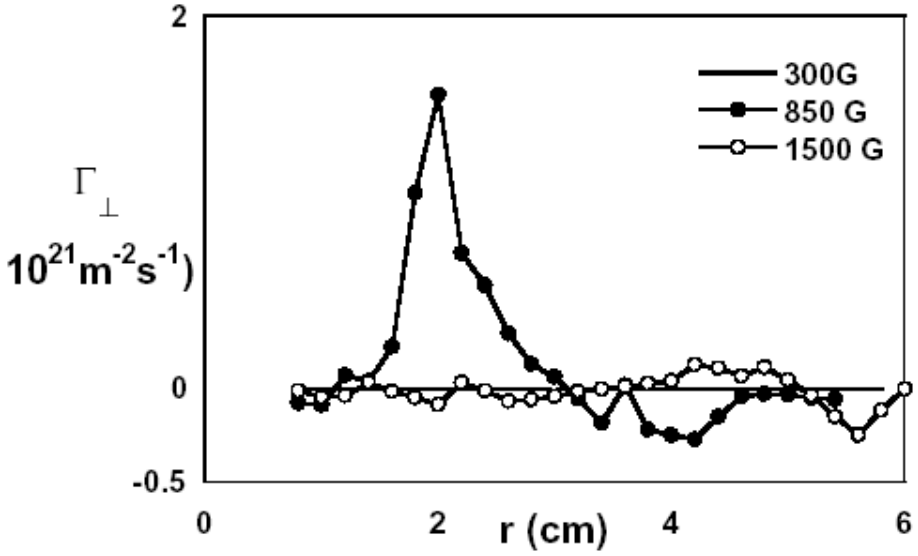

Fig. 13. Measured radial flux vs. radius at three magnetic fields [Ref. 33].

A similar experiment was later performed by Tynan et al.[35,36] The apparatus was a helicon discharge 10 cm in diameter, injected into a larger chamber. The field lines terminated on an insulator at one end and on floating metal rings at the other (for later controlling the radial E-field). Their radial profiles of n, T_e, and plasma potential ϕ are shown in Fig. 14. The maximum gradients are around 3 cm, near the radius of the injected plasma.

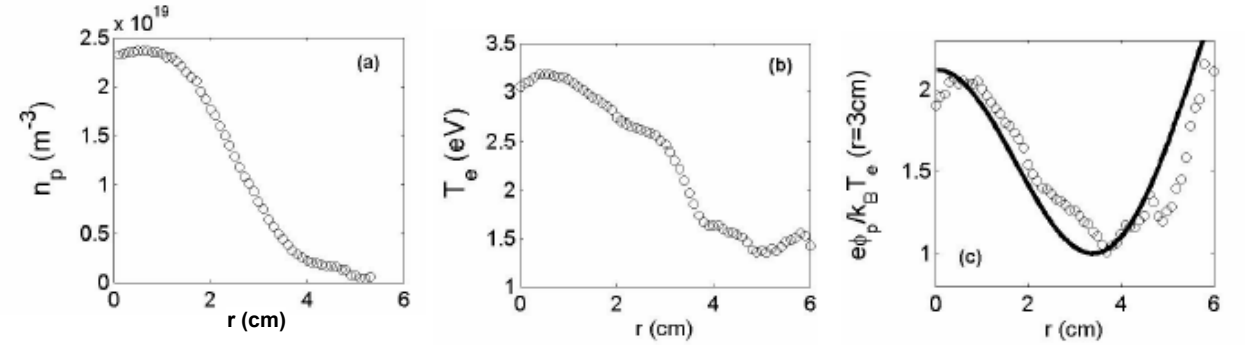

Fig. 14. Density, T_e, and normalized space potential vs. radius. [Ref. 35]

The potential reverses slope there, indicating a region of large electric field shear. This shape was attributed to a turbulence theory, but in a system with endplates, it is difficult to apply such a theory with certainty. Figure 15 shows radial profiles of the density and potential fluctuations, as well as the $<\tilde{n}\ \tilde{\phi}>$ flux Γ, measured in the usual way. This peaks near the maximum ∇n_0. The diffusivity D_r is computed by dividing Γ by ∇n_0. As in Light's experiment, the oscillatory transport does not extend all the way to the radial wall. In this case, the wall is some distance away, so it is clear that the plasma, initially transported radially, eventually is lost by axial flow.

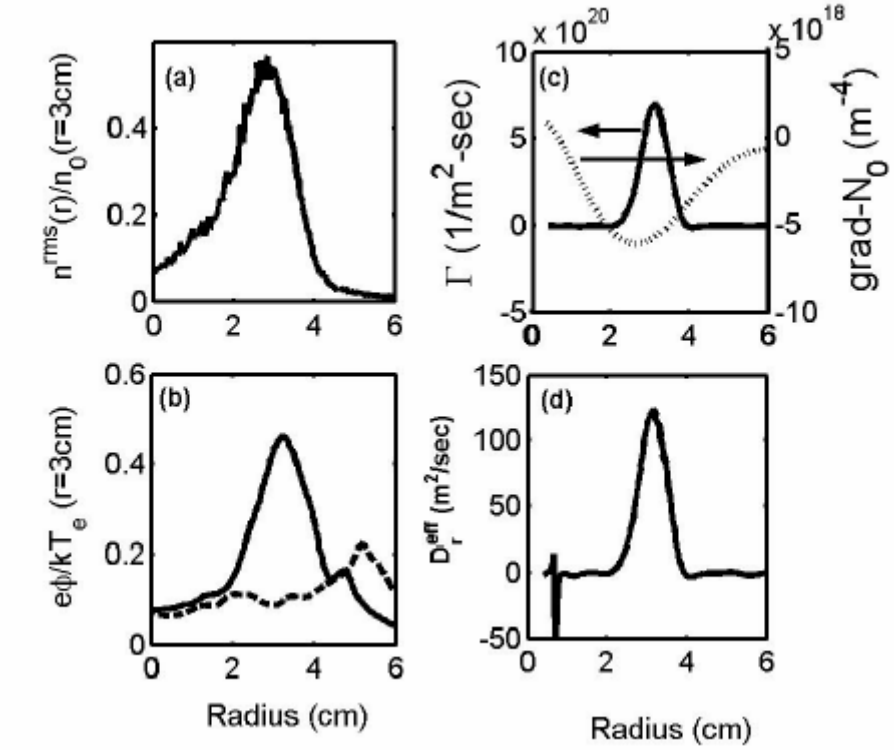

Fig. 15. Radial profiles of (a) normalized density fluctuations, (b) normalized potential fluctuations, (c) radial flux from correlations with the density gradient, and (d) computed diffusivity. [Ref. 35]

III. Parametric instabilities in helicon discharges

The mechanism by which rf energy from a helicon antenna is transferred to the plasma has been a major puzzle, this being so efficient in helicon discharges. The currently accepted picture is that the antenna excites a helicon wave, whose energy is concentrated near the axis, and the helicon then couples, through currents or charges induced on the radial boundary, to a Trivelpiece-Gould (TG) mode near the periphery. The TG mode is an electron cyclotron wave confined to a cylinder. It is electrostatic, travels slowly inwards, and is rapidly damped by collisons. Thus, though the helicon itself is weakly damped, it can transfer its energy to plasma heat via this mode-coupling mechanism. This is illustrated in Fig. 16. The TG mode has been

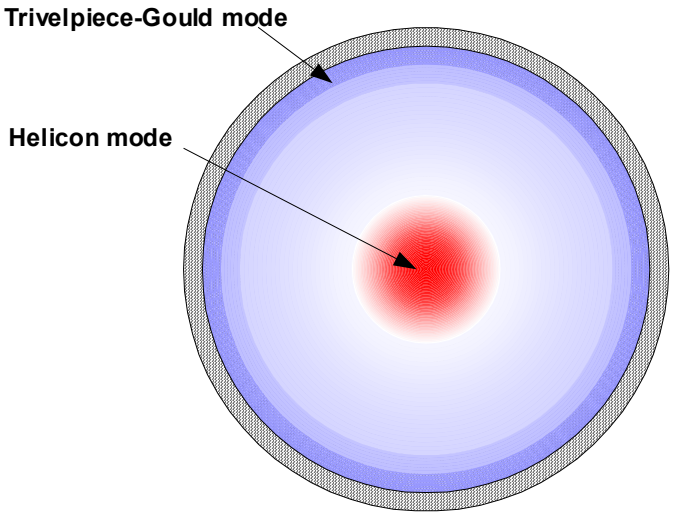

Fig. 16. Illustration of the coupled helicon and Trivelpiece-Gould waves.

detected experimentally, and computations show that the TG mode accounts for most of the rf energy absorption. However, there may also be other mechanisms. Most mesurements can be made only downstream from the antenna, where the rf pickup is not so severe. Excitation of ion acoustic waves, for instance, in the plasma under the antenna has been suggested; but these

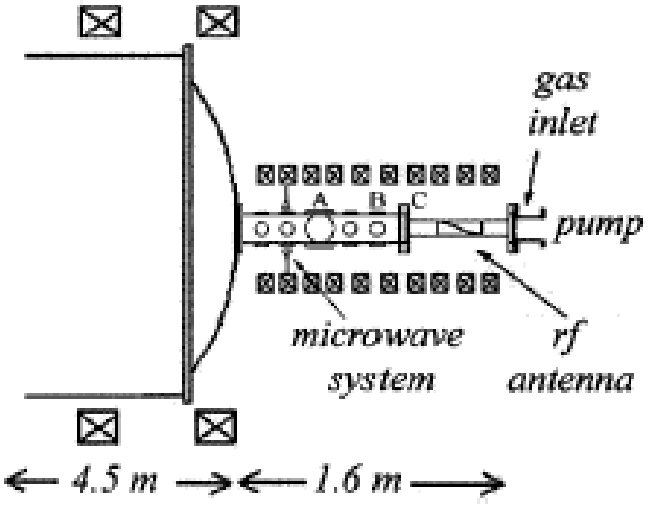

Fig. 17. Helicon experiment of Kline et al. [Ref. 38]. Measurements were made in port A downstream from the source region.

waves have not been detected. At least two groups, however, have detected low-frequency waves in the downstream region. Selenin et al.[37] and Kline et al.[38] were the first to report this, the latter using the machine shown in Fig. 17. In the West Virginia experiment, the helicon waves were launched at 11 MHz, and low-frequency signals at f_1 (~1MHz) were detected by

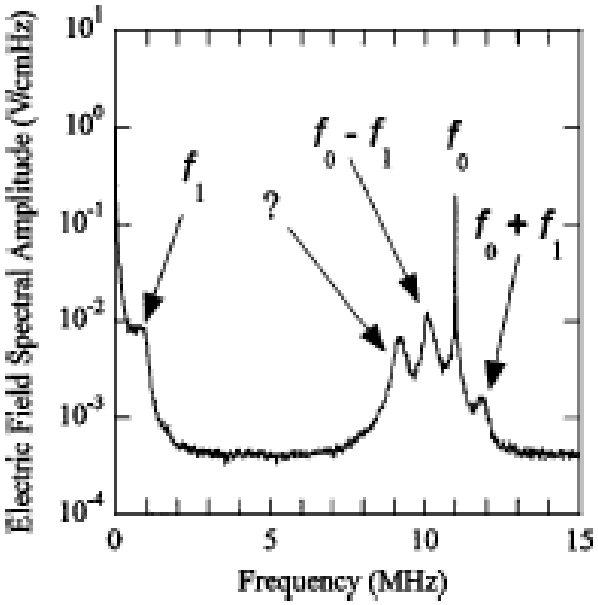

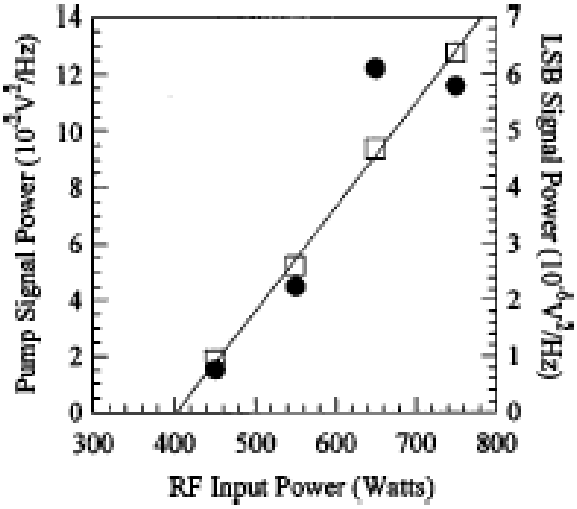

Fig. 18 (left). Spectrum of electrostatic oscillations [Ref. 38].
Fig. 19 (right). Power in the pump (□) and the lower sideband (●) *vs*. input power [Ref. 38].

both electrostatic and magnetic probes. In the spectrum shown in Fig. 18, upper and lower (LSB) sidebands of the pump f_0 were seen at $f_0 \pm f_1$. There was an unidentified wave at ~9 MHz. It was suggested that f_1 was an ion acoustic (IA) wave, and the LSB was a lower-hybrid (LH) wave, and that these were parametrically excited. It is also possible that it was the unknown peak that was the LH wave, and that the sidebands were created by modulation of the pump by the IA wave. This possibility is supported by Fig. 19, which shows that the LSB power grows linearly with P_{rf}, and not exponentially as in a parametric instability. However, there is then the question of what excites the LH wave. Whether or not parametric decay occurred here is not clear. Ion-cyclotron sidebands possibly connected with parametric instabilities have also been seen by Boswell and co-workers[39,40], but the excitation physics was not discussed.

The situation has been clarified by more recent work done by the group of M. Krämer in Bochum, Germany. This experiment[41] had a number of refinements. First, the rf was double-pulsed, with the first pulse creating the plasma, and the second, smaller pulse creating a test wave in the afterglow of a pre-formed plasma. Second, low-frequency fluctuations were detected by a) an electrostatic probe array, b) capacitive probes, and c) microwave backscatter. Third, auto- and cross-correlation techniques were extensively used to bring the signals out of the background. By fitting the downstream amplitude to an exponential, the axial damping rate Im(k_z) could be determined. Figure 20 shows that this increases with rf power, indicating a power-dependent damping mechanism away from the antenna. Frequency spectra measured with electrostatic probes in Fig. 21 show a low-frequency component and the sidebands it generates on the pump signal at 13.56 MHz. The sideband enlarges and broadens with P_{rf}. Figure 22 shows that the low-frequency signal is more of a density than a potential fluctuation, as would be expected of ion acoustic waves. Further evidence of IA waves is found in the wavenumber measurement by cross-correlation. Figure 23 shows the components of the

propagation constant of the low-frequency wave. The wave propagates primarily in the θ direction, and it reverses phase on the other side of the discharge, so it is an $m = 1$ mode. Furthermore, the value of kc_s yields an electron temperature of 2.8 eV, agreeing with the measured KT_e of 3 eV.

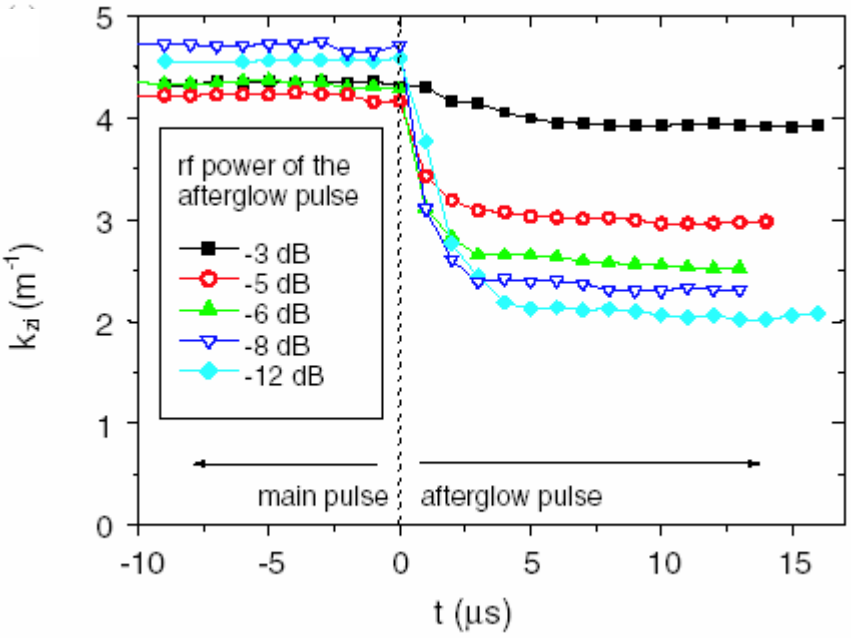

Fig. 20. Axial damping rate Im(k_z) vs. time, showing an increase with P_{rf} [Ref. 41]. These pulsed experiments were done with $P_{rf} \leq 2$kW at 13.56 MHz, $p = 1.5$–4.5 mTorr, $B_0 \leq 1000$ G, yielding $n \leq 2 \times 10^{13}$ cm^{-3} and $KT_e \approx 3$eV.

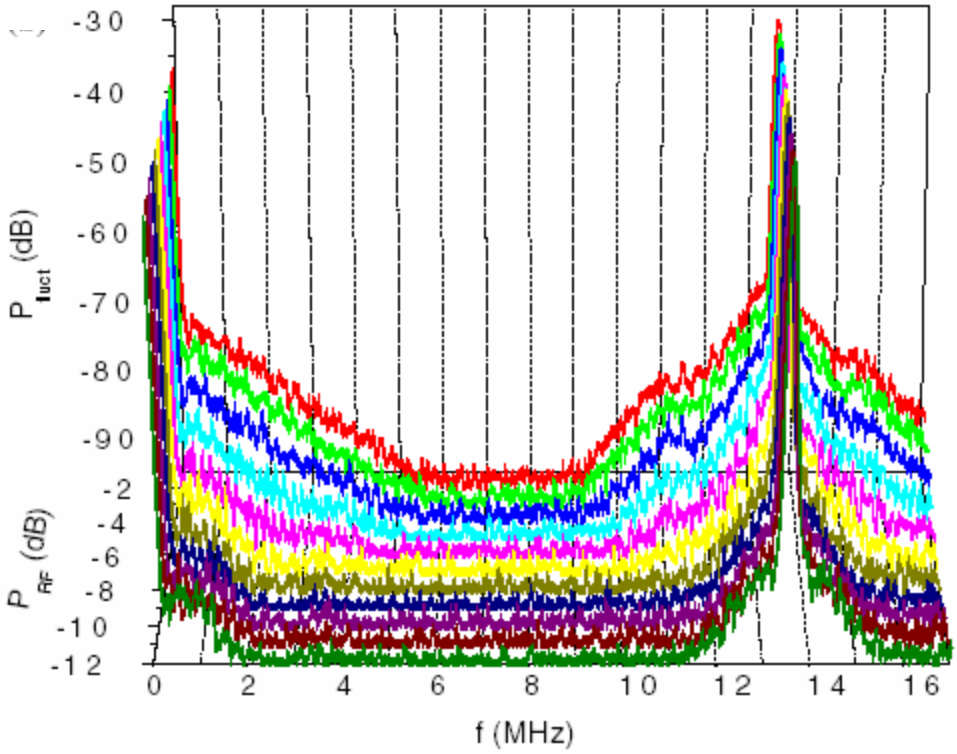

Fig. 21. Electrostatic-probe spectra at various rf powers, increasing upwards [Ref. 41].

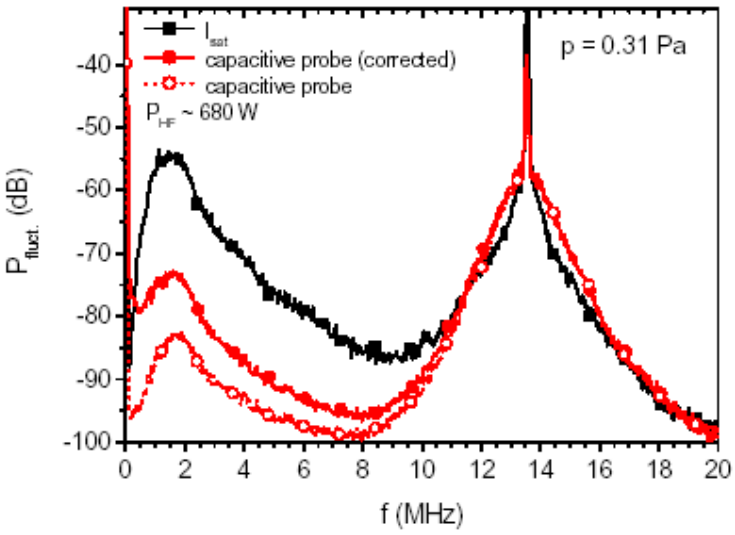

Fig. 22. Frequency spectra taken with electrostatic (top curve) and capacitive (middle curve) probes. The bottom curve is uncorrected for the frequency response of the capacitive probe [Ref. 41].

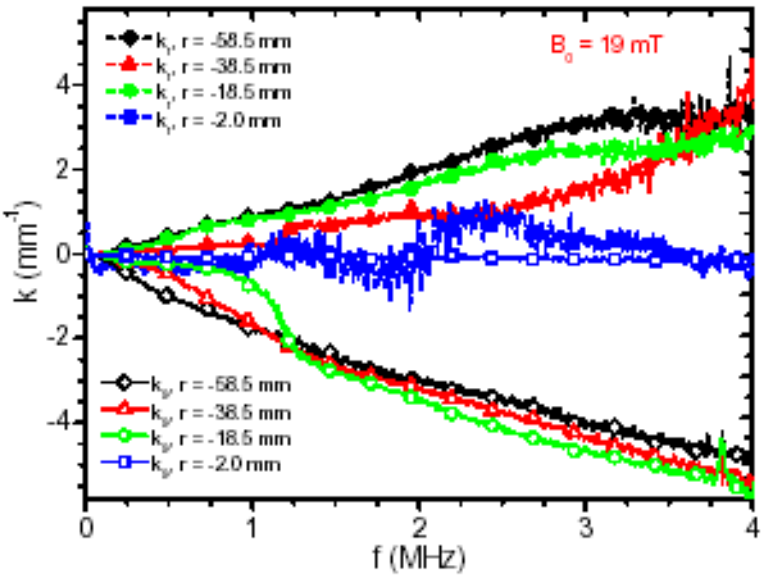

Fig. 23. Propagation constants k_r and k_θ of the low-frequency wave [Ref. 41].

The other daughter wave in the parametric decay is the Trivelpiece-Gould mode, which by definition has the same frequency as the sideband caused by the IA wave. Thus the decay scheme is as in Fig. 24, which satisfies frequency and k-matching. Here $\mathbf{k}_0$ is the helicon wave, $\mathbf{k}_1$ the IA wave, and $\mathbf{k}_2$ the TG wave. The last relation was verified by measuring the signs of $\mathbf{k}$ in the IA and TG waves, and they were indeed reversed. Figure 25 shows direct measurements of the growth rate γ using microwave backscatter. These agree with calculations of γ from parametric instability theory. That this instability actually takes energy from the helicon wave can be seen from Fig. 26, which shows that both the LF power and the helicon damping rate grow almost exponentially with rf power.

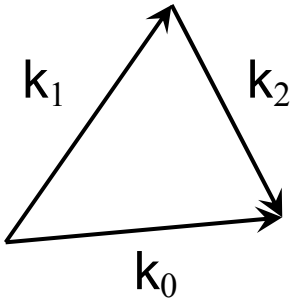

$$\omega_0 = \omega_1 + \omega_2$$

$$k_0 = k_1 + k_2 \sim 0$$

$$k_1 \sim -k_2$$

Fig. 24. Parametric matching conditions.

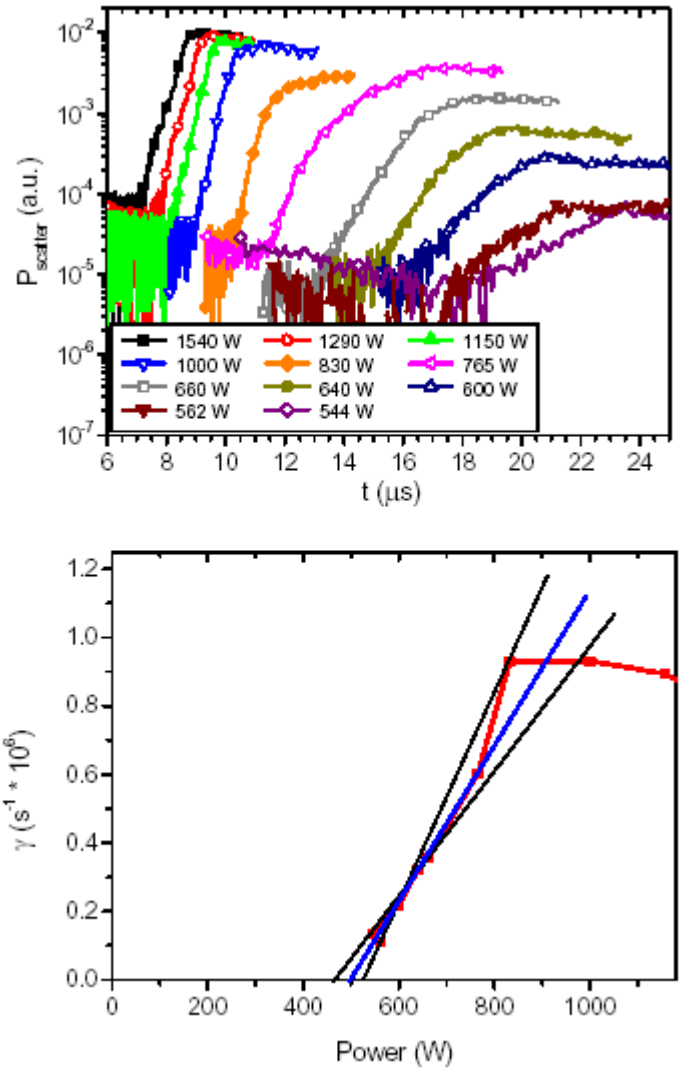

Fig. 25. Direct measurements of wave growth using microwave backscatter at various rf powers. The bottom graph shows the measured growth rates compared with the theoretically computed range. [Ref. 41]

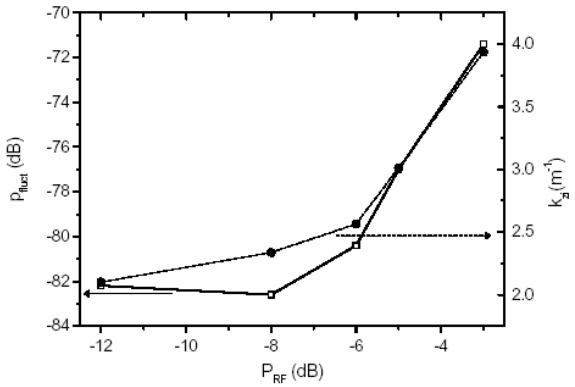

Fig. 26. Nonlinear increase of low-frequency power and helicon damping. [Ref. 41]

This experiment showed definitively that a nonlinear damping mechanism exists in helicon discharges: namely, the parametric decay of the helicon wave into a Trivelpiece-Gould mode and an ion acoustic wave. This occurs in the middle of the column, not at the edge, and is detected downstream from the antenna. Since the waves are weak in the downstream region, the energy transfer is not significant in the overall transfer of energy from the antenna to the plasma. However, what is measured may be the effects of a stronger interaction in the antenna region, propagated downstream where they could be detected.

IV. Conclusion

In these three examples, we hoped to show that interesting and challenging physics can be found in partially ionized plasmas. There is a link between the disciplines of high- and low-temperature plasmas.

FIGURE CAPTIONS

Fig. 1. Radial profiles of density, electron temperature, and the rf B_z field in the apparatus of Fig. 2. [Ref.1]

Fig. 2. Schematic of a commercial processing reactor with a side-mounted antenna.

Fig. 3. Trajectory of an electron through four rf cycles [Ref. 1]. Assumed parameters: f = 6.78 MHz, skin depth = 3.1 cm, tube radius = 15 cm, sheath drop = 20 V, p = 10 mTorr (argon), and KT_e = 3 eV.

Fig. 4. Energy of the test electron computed with (○)and without (♦) the Lorentz force, for an applied rf E-field of 8 V/cm at 6.78 MHz. [Ref. 1]

Fig. 5. Distribution of electron positions after 32,000 2-nsec time steps. [Ref. 1]

Fig. 6. Histogram of the density distibution of Fig. 5, together with the experimental curve of Fig. 1. [Ref. 1]

Fig. 7. Calculated energy distributions in each sector, compared with a Maxwellian (curve), on a log-log scale. The radii covered by each sector are shown in the inset. [Ref. 1]

Fig. 8. Radial profiles of rf B_z field at various pressures. The bottom curve is a computed fit to the 20-mTorr data [Ref. 1]. Experimental conditions: 400 W at 2 MHz, 5–20 mTorr of Ar.

Fig. 9. A detached current ring and its B-field in a plasma. The field of the external antenna has been added to that generated by the current ring [Ref. 1]. Assumed conditions: $n = 8 \times 10^{10}$ cm^{-3} plasma with p = 10 mTorr, KT_e = 3 eV, and f = 2 MHz.

Fig. 10. Helicon density on axis for various gases vs. magnetic field. [Ref. 32]

Fig. 11. Bottom: density vs. B_0 measured in neon. Top: frequency spectrum of probe signals on same scale. [Ref. 32]

Fig. 12. Top: Computed growth rate vs. $\mathbf{B}_0$ compared with measured potential and density fluctuation amplitudes. Bottom: Calculated and measured radial transport fluxes. [Ref. 33]

Fig. 13. Measured radial flux vs. radius at three magnetic fields [Ref. 33].

Fig. 14. Density, T_e, and normalized space potential vs. radius. [Ref. 35]

Fig. 15. Radial profiles of (a) normalized density fluctuations, (b) normalized potential fluctuations, (c) radial flux from correlations with the density gradient, and (d) computed diffusivity. [Ref. 35]

Fig. 16. Illustration of the coupled helicon and Trivelpiece-Gould waves.

Fig. 17. Helicon experiment of Kline et al. [Ref. 38]. Measurements were made in port A downstream from the source region.

Fig. 18 (left). Spectrum of electrostatic oscillations [Ref. 38].

Fig. 19 (right). Power in the pump (□) and the lower sideband (●) *vs*. input power [Ref. 38].

Fig. 20. Axial damping rate Im(k_z) vs. time, showing an increase with P_{rf} [Ref. 41]. These pulsed experiments were done with $P_{rf} \leq$ 2kW at 13.56 MHz, p = 1.5–4.5 mTorr, $B_0 \leq$ 1000 G, yielding $n \leq 2 \times 10^{13}$ cm^{-3} and $KT_e \approx$ 3eV.

REFERENCES

[1] J.D. Evans and F.F. Chen, "Nonlocal power deposition in inductively coupled plasmas," Phys. Rev. Lett. **86**, 5502 (2001).

[2] R.A. Demirkhanov, I.Ya. Kadysh, and Yu. S. Khodyrev, "Skin effect in a high frequency ring discharge," Soviet Phys. JETP **19**, 791 (1964).

[3] M.J. Kofoid and J.M. Dawson, "Anomalous skin depth in a gaseous plasma," Phys. Rev. Lett. **17**, 1086 (1966).

[4] B. Joye and H. Schneider, Title not available, Helv. Phys. Acta **51**, 804 (1978).

[5] E.S. Weibel, "Anomalous skin effect in a plasma," Phys. Fluids **10**, 741 (1967).

[6] Yu. S. Sayasov, Title not available , Helv. Phys. Acta **52**, 288 (1979).

[7] V.I. Kolobov and D.J. Economou, "The anomalous skin effect in gas discharge plasmas," Plasma Sources Sci. Technol. **6,** R1 (1997).

[8] V.I. Kolobov and V.A. Godyak, "Nonlocal electron kinetics in collisional gas discharge plasmas," IEEE Trans. Plasma Sci. **23**, 503 (1995).

[9] V. Godyak, "Plasma phenomena in inductive discharges," Plasma Phys. Control. Fusion **45**, A399 (2003).

[10] V.A. Godyak, R.B. Piejak, B.M. Alexandrovich, and V.I. Kolobov, "Experimental evidence of collisionless power absorption in inductively coupled plasmas," Phys. Rev. Lett. **80**, 3264 (1998).

[11] S. Takechi, and S. Shinohara, "Role of electron thermal motion in evanescent electromagnetic wave structure of inductively coupled plasma," Jpn. J. Appl. Phys. **38**, L148 (1999).

[12] V.A. Godyak, B.M. Alexandrovich, and V.I. Kolobov, "Lorentz force effects on the electron energy distribution in inductively coupled plasmas," Phys. Rev. E **64,** 026406 (2001).

[13] Yu.O. Tyshetskiy, A.I. Smolyakov, and V.A. Godyak, "On nonlocal heating in inductively coupled plasmas," Plasma Sources Sci. Technol. **11** 203 (2002).

[14] V.A. Godyak and V.I. Kolobov, "Negative power absorption in inductively coupled plasma," Phys. Rev. Lett. **79**, 4589 (1997).

[15] V.A. Godyak, R.B. Piejak, and B.M. Alexandrovich, "Observation of second harmonic currents in inductively coupled plasmas," Phys. Rev. Lett. **83**, 1610 (1999).

[16] V. Godyak, B. Alexandrovich, R. Piejak, and A. Smolyakov, "Nonlinear radio-frequency potential in an inductive plasma," Plasma Sources Sci. Techn. **9**, 541 (2000).

[17] V. Godyak, R. Piejak, B. Alexandrovich, and A. Smolyakov, "Observation of the ponderomotive effect in an inductive plasma," Plasma Sources Sci. Technol. **10**, 459 (2001).

[18] A.I. Smolyakov, V. Godyak, and Y. Tyshetskiy, "Effect of the electron thermal motion on the ponderomotive force in inductive plasma," Phys. Plasmas **8**, 3857 (2001).

[19] A.I. Smolyakov, V. A. Godyak, and Y. O. Tyshetskiy, "Nonlinear effects in inductively coupled plasmas, Phys. Plasmas **10**, 2108 (2003).

[20] R.B. Piejak and V.A. Godyak, "Second harmonic and ponderomotive forces acting on electrons in an inhomogeneous radio frequency field of an inductive discharge," Appl. Phys. Lett. **76**, 2188 (2000).

[21] A. Smolyakov, V. Godyak, and A. Duffy, "On nonlinear effects in inductively coupled plasmas," Phys. Plasmas **7**, 4755 (2000).

[22] F.F. Chen, *Introduction to Plasma Physics and Controlled Fusion*, 2nd ed., Vol. 1, p 306 (Plenum Press, New York, 1984).

[23] F.F. Chen, "Collisional, magnetic, and nonlinear skin effect in RF plasmas," Phys. Plasmas **8**, 3008 (2001).

[24] V.A. Godyak and V.I. Kolobov, "Effect of collisionless heating on electron energy distribution in an inductively coupled plasma," Phys. Rev. Lett. **81**, 369 (1998).

[25] V.A. Godyak, R.B. Piejak, and B.M. Alexandrovich, "Electron energy distribution function measurements and plasma parameters in inductively coupled argon plasma," Plasma Sources Sci. Technol. **11,** 525 (2002).

[26] G. DiPeso, V. Vahedi, D.W. Hewett, and T.D. Rognlien, "Two-dimensional self-consistent fluid simulation of radio frequency inductive sources," J. Vac. Soc. Technol. A **12**, 1387 (1994).

[27] G. DiPeso, T.D. Rognlien, V. Vahedi, and D.W. Hewett, "Equilibrium profiles for RF-plasma sources with ponderomotive forces," IEEE Trans. Plasma Sci. **23**, 550 (1995).

[28] R.H. Cohen and T.D. Rognlien, "Induced magnetic-field effects in inductively coupled plasmas," Phys. Plasmas **3**, 1839 (1996).

[29] R.H. Cohen and T.D. Rognlien, "Electron kinetics in radio-frequency magnetic fields of inductive plasma sources ," Plasma Sources Sci. Technol. **5**, 442 (1996).

[30] V.I. Kolobov, D.P. Lymberopoulos, and D.J. Economou, "Electron kinetics and non-Joule heating in near-collisionless inductively coupled plasmas." Phys. Rev. E **55**, 3408 (1997).

[31] I.D. Kaganovich, O.V. Polomarov, and C.E. Theodosiou, "Landau damping and anomalous skin effect in low-pressure gas discharges: Self-consistent treatment of collisionless heating," Phys. Plasmas **11**, 2399 (2004).

[32] M. Light, F.F. Chen, and P.L. Colestock, "Quiescent and unstable regimes of a helicon plasma," Plasma Sources Sci. Technol. **11**, 273 (2002).

[33] M. Light, F.F. Chen, and P.L. Colestock, "Instability driven radial transport in a helicon plasma," UCLA LTP-101 (January, 2001).

[34] M. Light, F.F. Chen, and P.L. Colestock, "Low frequency electrostatic instability in a helicon plasma," Phys. Plasmas **8**, 4675 (2001).

[35] G.R. Tynan, M.J. Burin, C. Holland, G. Antar, and P.H. Diamond, "Radially sheared azimuthal flows and turbulent transport in a cylindrical helicon plasma device," Plasma Phys. Control. Fusion **46**, A373 (2004).

[36] M.J. Burin, G.R. Tynan, G.Y. Antar, N.A. Crocker, and C. Holland, "On the transition to drift turbulence in a magnetized plasma column," Phys Plasmas **12**, 052320 (2005).

[37] V.L. Selenin, M. Krämer, N. M. Kaganskaya and B. Lorenz, "Investigation of a parametric instability in a helicon discharge by cross-correlation enhanced-scattering", Proc. 29th EPS Conference on Plasma Physics and Controlled Fusion, Montreux, 2002, Vol. 26B, p. 2.024.

[38] J.L. Kline and E.E. Scime, "Parametric decay instabilities in the HELIX helicon plasma source," Phys. Plasmas **10**, 135 (2003).

[39] R. W. Boswell, O. Sutherland, C. Charles, J.P. Squire, F.R. Chang-Diaz, T.W. Glover, V.T. Jacobson, D.G. Chavers, R.D. Bengtson, E.A. Bering III, R.H. Goulding, and M. Light, "Experimental evidence of parametric decay processes in the variable specific impulse magnetoplasma rocket (VASIMR) helicon plasma source," Phys. Plasmas **11**, 5125 (2004).

[40] O. Sutherland, M. Giles, and R. Boswell, Ion Cyclotron Production by a Four-Wave Interaction with a Helicon Pump," Phys. Rev. Lett. **94**, 205002 (2005).

[41] B. Lorenz, M. Krämer, V.L. Selenin, and Yu.M. Aliev, "Excitation of short-scale fluctuations by parametric decay of helicon waves into ion–sound and Trivelpiece–Gould waves," Plasma Sources Sci.Technol. **14,** 623 (2005).